

Electronic analogue of Fourier optics with massless Dirac fermions scattered by quantum dot lattice

Partha Sarathi Banerjee, Rahul Marathe, and Sankalpa Ghosh*

Department of Physics, Indian Institute of Technology Delhi, Hauz Khas, New Delhi 110016

The field of electron optics exploits the analogy between the movement of electrons or charged quasiparticles, primarily in two-dimensional materials subjected to electric and magnetic (EM) fields and the propagation of electromagnetic waves in a dielectric medium with varied refractive index. We significantly extend this analogy by introducing an electronic analogue of Fourier optics dubbed as Fourier electron optics (FEO) with massless Dirac fermions (MDF), namely the charge carriers of single-layer graphene under ambient conditions, by considering their scattering from a two-dimensional quantum dot lattice (TDQDL) treated within Lippmann-Schwinger formalism. By considering the scattering of MDF from TDQDL with a defect region, as well as the moiré pattern of twisted TDQDLs, we establish an electronic analogue of Babinet's principle in optics. Exploiting the similarity of the resulting differential scattering cross-section with the Fraunhofer diffraction pattern, we construct a dictionary for such FEO. Subsequently, we evaluate the resistivity of such scattered MDF using the Boltzmann approach as a function of the angle made between the direction of propagation of these charge-carriers and the symmetry axis of the dot-lattice, and Fourier analyze them to show that the spatial frequency associated with the angle-resolved resistivity gets filtered according to the structural changes in the dot lattice, indicating wider applicability of FEO of MDF.

I. INTRODUCTION

The unique transmission properties of massless Dirac fermions (MDF) in graphene through potential landscapes created by a variety of electromagnetic (EM) fields, particularly in the ballistic regime [1–6], and its similarity with the light transmission through an optical medium with unconventional dielectric properties such as metamaterials [7, 8] make graphene an excellent material to realize electron optics-based devices in a solid state system. The realisation of negative refraction [9], chiral Veselago lensing of MDF in two [10] and three dimensions [11], tunable Veselago interference in a bipolar graphene microcavity [12], creation of a Dirac fermion microscope [13], collimation [14–16], and different type of interferometers [17–20], gate tunable beam-splitter of such MDF [21], Fabry-pérot resonator in graphene/hBN moiré super-lattice [22], gradient index electron optics in graphene p-n junction [23], Mie scattering in graphene, [24] are few milestones in this direction. Most of these experimental and theoretical studies are based on theoretical modelling of Dirac fermions scattered by the potential, which are constant in one direction [1–6, 14, 25–30], and hence limit the range of applications in this fast-growing field.

New possibilities can emerge if the EM potential that can scatter such MDF can vary along both transverse directions. For example, in the well-known Fraunhofer diffraction, when the observation point is significantly distant(z) from the diffracting object dubbed as the far-field case, the field distribution at the observation plane is the Fourier transform of the aperture function($A(x', y')$) [31–37]. The diffracting object is positioned at the front

focal plane of a lens, resulting in the generation of a Fourier transform of the object at the back focal plane of the lens, thereby satisfying the conditions for the Fraunhofer approximation($z \gg [x'^2 + y'^2]_{\max} / \lambda$) as depicted in Fig. 1 and described in TABLE I. The framework of Fourier optics was introduced in a seminal work by P. M. Duffieux [31] and later elucidated in detail in the classic textbook of Born and Wolf [36]. In this work we show that an electronic analogue of this situation can be realized in a fully two-dimensional (2D) scattering model, where the scattering of such MDF takes place from a two-dimensional superlattice potential that can be realised by creating an electrostatically defined array of quantum dots (QDs) on the surface of single-layer graphene [38–48].

The scattering of electrons by gate-defined QDs with sharp p-n junction has been theoretically studied using the Mie scattering [24] and multiple scattering theory [45–47]. In comparison to those approaches, in this paper using first Born approximation, we show that, the differential scattering cross-section (DSC) of a scattering potential is proportional to the Fourier transform of the potential profile. This is analogous to intensity in the back focal plane in the case of Fraunhofer diffraction pattern [31, 36]. However, due to Klein tunneling and absence of back-scattering, the MDFs in graphene are mainly transmitted towards the forward region which makes graphene scattering interesting. Particularly in the inset of Fig. 1 (b) we show the differential scattering cross-section from a single QD forms a cardioid like pattern which combine the effects of Mie scattering and Klein tunneling for the gaussian QD we are considering. In this framework we showed how using dc-resistivity, an experimentally measurable quantity which is dependent on this DSC, we can analyze the properties of the scattering potential in a way that is reminiscent of optical image processing. While in optical image processing a

* Corresponding author. Email: sankalpa@physics.iitd.ac.in

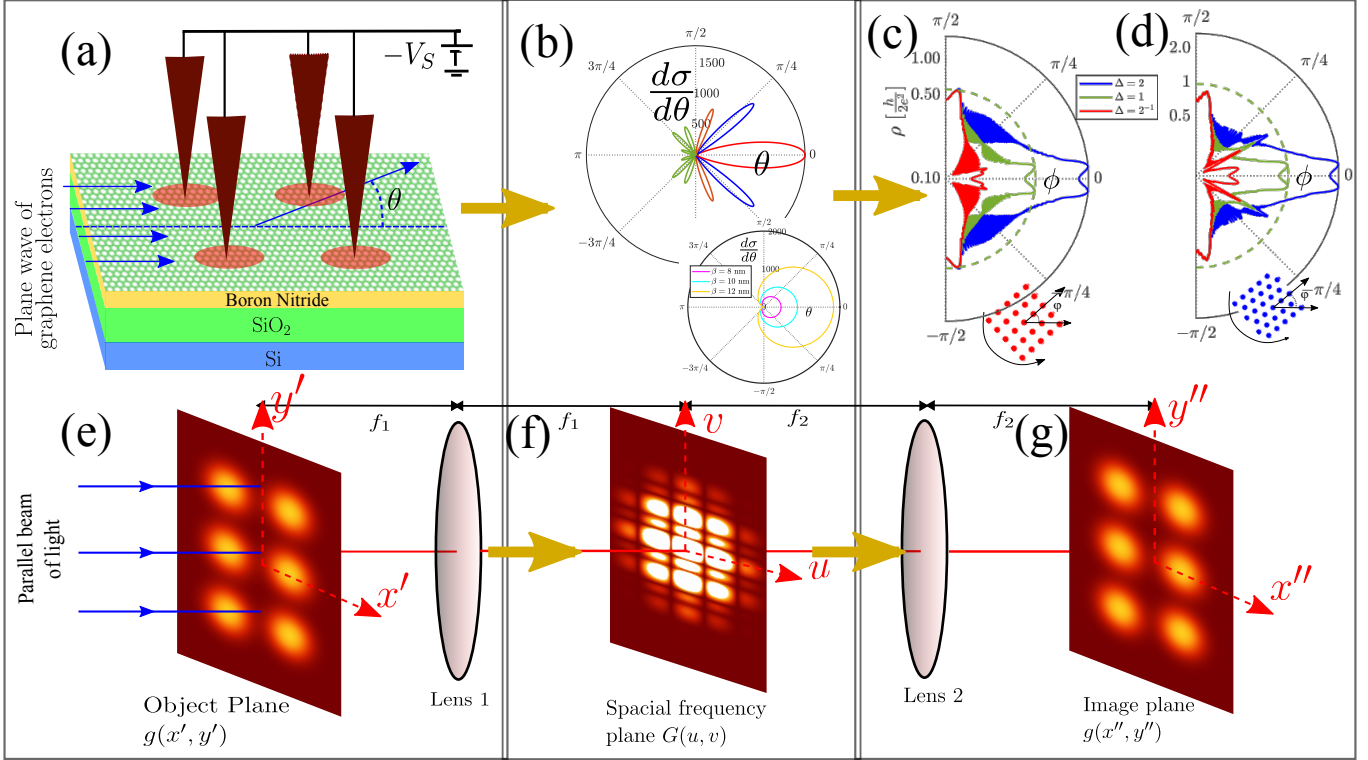


FIG. 1: (a) The schematic diagram of a plane wave (direction shown in blue arrows) of charge carriers in ballistic graphene that are modelled as MDF under ambient conditions, getting scattered by a two-dimensional array of Gaussian quantum dot (QD) potentials created by STM tips. (b) The polar plot of the DSC for a square lattice of QDs as given by Eq. (3a), of dimension $N_1 = 10, N_2 = 0$ and orientation $\phi = 0$. The central maxima at $\theta = 0$ is multiplied with 1.6×10^{-3} for better visibility. The first maxima on both sides are multiplied by 0.8×10^{-2} . The second ones are multiplied by 0.32 for better visibility with respect to the other smaller peaks. In the inset we have shown the differential scattering cross section for a single QD for differential values of β . In (c) and (d) the angle-resolved dc-resistivity of the system parallel to the direction of propagation of the incoming plane wave of graphene electrons is plotted under this scattering potential rotated at an arbitrary angle. The resistivity pattern for square and hexagonal lattices of QDs is shown in (c) and (d) for $N_2 = 100$. The resistivity at $\phi = 0^\circ$ and 90° is the same for the square lattice but not in the case of the hexagonal lattice. In Figs. (e)-(g) we compare the process described in (a)-(d) with the two-dimensional optical spatial frequency processor, whereas a short thesaurus listing various analogue quantities in these two systems is given in TABLE I. In (e) we show that the object is positioned in the front focal plane of lens 1. The Fourier transform of the object distribution is found in the back focal plane of lens 1 as shown in (f). This plane is called spatial frequency plane [32, 35]. At the image plane in (g) the object distribution is recovered.

second lens is used to reconstruct the image (depicted in Fig. 1), similar thing is however not possible in our system. To overcome this limitation we have introduced another degree of freedom, rotation angle ϕ , which is the angle between the direction of propagation of incident plane wave and the symmetry axis of the two dimensional QD lattice (TDQDL). By doing Fourier analysis of this dc resistivity we can get information about the symmetry and lattice configuration, lattice constant, size and location of defect of the scattering lattice. In a moiré pattern of two TDQDL, we have shown that the Fourier analysis can give us the information about the symmetries (moiré pattern of two hexagonal/square lattices) and commensurate conditions.

Particularly in the ballistic regime, with the Fermi ve-

locity $v_F \sim 10^6 \text{ m s}^{-1}$, the mean free path of the charge carriers in graphene are several microns [49–51] \gg the size of ($\sim 10 \text{ nm}$) [52] such scatterers, and the Fraunhofer criterion is satisfied [51, 53, 54]. In order to observe a clear diffraction pattern in the optical case, the aperture length must be comparable to the wavelength of light [36, 37]. This is ensured in our analogue solid-state system by considering that the lattice spacing ($\sim 40 \text{ nm}$) and characteristic length ($\sim 10 \text{ nm}$) of each barrier [52] in this QD lattice are smaller than the de Broglie wavelength calculated from the incident energy of the graphene electrons ($\sim 30 - 40 \text{ meV}$) [20]. Also, for the typical energy range we have considered, the wavevector of the MDF is much smaller than the Fermi wave vector, i.e., $k \ll k_F$, eliminating the possibility of inter-valley

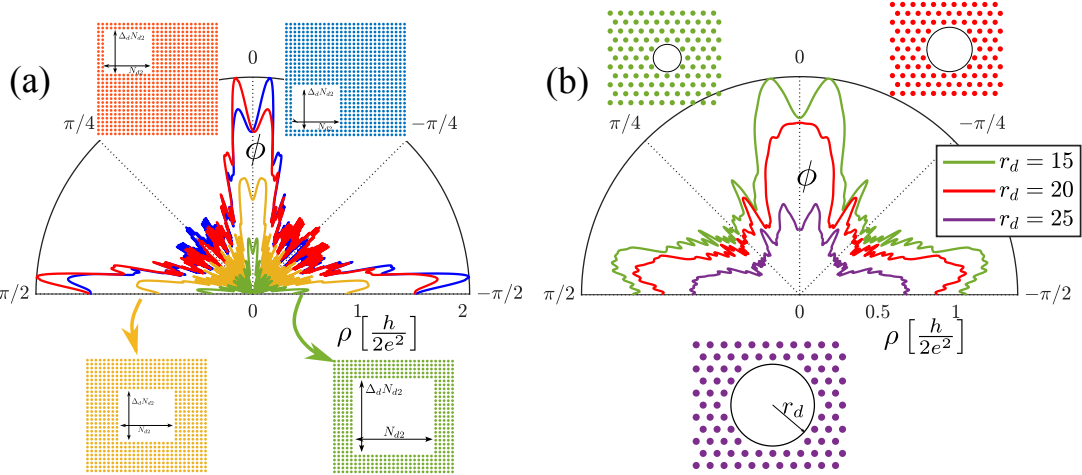


FIG. 2: Resistivity pattern for (a) square QD lattice of size $N_2 = 200$ and $\Delta = 1$ with square defect region with different sizes and (b) hexagonal QD lattice of size $N_2 = 61$ and $\Delta = 1$ with circular defect region of different radii. In (a), The resistivity pattern is symmetric on both sides of $\phi = 0$ only when the defect region is centred at the origin and for the blue curve, we have removed scatterers from $n_1 = 10$ to 110 and $n_2 = 10$ to 110. For the orange curve $n_1 = 10$ to 110 and $n_2 = 90$ to 190. In (b), the defect region is placed in the centre of the original QD lattice. Here, the resistivity pattern is symmetric on both sides of $\phi = 0$.

scattering. Thus, the problem can be modelled by starting with the single-valley non-interacting Hamiltonian of the massless Dirac fermions in single-layer graphene given by $\hat{H}_0 = v_F \sigma \cdot \mathbf{p}$. Such a two-dimensional QD lattice (TDQDL) serves as two-dimensional grating for the incident charge carriers for graphene, leading to an electronic analogue of Fraunhofer diffraction pattern, but with an important distinction characterising the absence of backscattering for such MDF [55, 56]. In SEC. II, we discuss the scattering of MDF from three prototype combinations of such dot lattices and lay down the basic premises of our theoretical approach.

II. THEORY

The scattered state of such MDF $|\Psi_{\mathbf{k}}\rangle$ from an arbitrary scattering potential V can be obtained by finding out the solutions of $(\hat{H}_0 + \hat{V})|\Psi_{\mathbf{k}}\rangle = E|\Psi_{\mathbf{k}}\rangle$ using the Lippmann-Schwinger formalism and can be written as [57, 58]

$$\Psi_{\mathbf{k}}^{e,+}(\mathbf{r}) = \phi_{\mathbf{k}}^e(\vec{r}) - \frac{e^{ikr}}{2\hbar v_F} \sqrt{\frac{ik}{\pi r}} \left[\frac{1}{e^{i\theta}} \right] \langle \phi_{\mathbf{k}'}^e | \hat{T} | \phi_{\mathbf{k}}^e \rangle \quad (1)$$

where, transition operator $\hat{T} = \hat{V} + \hat{V}G_0^{\pm}\hat{V} + \hat{V}G_0^{\pm}\hat{V}G_0^{\pm}\hat{V} + \dots$ and \hat{G}_0^{\pm} is the Green's function defined as $\hat{G}_0^{\pm} = \lim_{\epsilon \rightarrow 0} [EI_2 - \hat{H}_0 \pm i\epsilon]$. $(\phi_{\mathbf{k}}^{e,h})$ are respectively free particle electron and hole solutions of $\hat{H}_0|\phi_{\mathbf{k}}\rangle = E|\phi_{\mathbf{k}}\rangle$. Here, \mathbf{k} is the wave-vector of the incident wave, $\mathbf{k}' = k\hat{r}$, θ is the angle between \mathbf{k} and \mathbf{k}' (see

Appendix A).

Realistic QD lattices that are heavily n-doped centres on a p-doped background [43, 44, 48] serves as scattering potential V as a Gaussian quantum dot array

$$V(\mathbf{r}) = \sum_n \left(\frac{V_0}{2\pi\beta^2} \right) e^{-\frac{1}{2}(\frac{\mathbf{r}-\mathbf{r}_n}{\beta})^2} \quad (2)$$

where \mathbf{r}_n s are the centres of each quantum dot where the Gaussian potential of width β forms its maxima. Such potential profile can be created using a needle-like electrode offered by an STM tip [40–44, 48], connected with a gate potential as shown in Fig. 1(a).

In experimental systems [40, 41, 43], these quantum dots are made on graphene/hBN heterostructures on SiO_2/Si substrate. The gate potential creates a stationary charge distribution in the insulating hBN underlayer, which creates the Gaussian potential profile in the graphene sheet. The SiO_2/Si substrate acts as a global back gate. To make an array of such QDs, the single electrode can be replaced by an array of such electrodes [42, 59–62].

For the type of potential profile depicted in Eq. (2), the premise for Fourier electron optics(FEO) with such MDF can be developed first by evaluating differential scattering cross-sections (DSC), which we did for three carefully chosen prototype combinations of such dot lattices and subsequently demonstrating their effect on transport. The DSCs evaluated respectively are:

TABLE I: Dictionary for various quantities in Fraunhofer diffraction in optics and their counterparts in scattering of MDF in graphene from a QD lattice

Fraunhofer diffraction in optics	Scattering of MDF in graphene from a QD lattice
Aperture profile in front focal plane, $A(\mathbf{r}')$	Scattering potential $V(\mathbf{r}')$
Field distribution at back focal plane, $G(u, v) = \frac{1}{\lambda f} \int \int dx' dy' g(x', y') e^{-i(ux' + vy')}$	Scattering amplitude $f(\theta) = -\sqrt{\frac{ik}{2\pi}} \frac{(1+e^{i\theta})}{2\hbar v_F} \int \int dx' dy' V(x', y') e^{i(q_x x' + q_y y')}$
Intensity $I = G(x, y) ^2$	Differential Scattering cross section $\frac{d\sigma}{d\theta} = f(\theta) ^2$
$u = \frac{2\pi x}{\lambda f}$ and $v = \frac{2\pi y}{\lambda f}$	$-q_x$ and $-q_y$
$\left(\frac{2\pi}{\lambda f}\right) \mathbf{r}$	$-\mathbf{q} = \mathbf{k}' - \mathbf{k}$
$\left(\frac{2\pi}{\lambda f}\right)^2 r^2$	$q^2 = 4k^2 \sin^2\left(\frac{\theta}{2}\right)$

$$\frac{d\sigma}{d\theta} = \frac{1}{4\hbar^2 v_F^2} \left(\frac{k}{\pi}\right) V_0^2 \mu(\theta) M_1^2(\theta, \phi) M_2^2(\theta, \phi), \text{ square lattice with dimension } (\Delta N_2 \times N_2),$$

and hexagonal lattice rotated in an angle ϕ (3a)

$$= \frac{kV^2\mu(\theta)}{4\pi\hbar^2 v_F^2} [M_1(N_2, \Delta, \phi, \mathbf{q}) M_2(N_2, \phi, \mathbf{q}) - M_1(N_{d2}, \Delta_d, \phi, \mathbf{q}) M_2(N_{d2}, \phi, \mathbf{q})]^2, \text{ square QD lattice with a defect region of rectangular shape} \quad (3b)$$

$$= \frac{kV^2\mu(\theta)}{4\pi\hbar^2 v_F^2} \left[M_1\left(N_2, \Delta, \phi - \frac{\delta}{2}, \mathbf{q}\right) M_2\left(N_2, \phi - \frac{\delta}{2}, \mathbf{q}\right) + M_1\left(N_2, \Delta, \phi + \frac{\delta}{2}, \mathbf{q}\right) M_2\left(N_2, \phi + \frac{\delta}{2}, \mathbf{q}\right) \right]^2$$

moiré pattern of two QD lattices (3c)

$M_1(N_2, \Delta, \phi, \mathbf{q}) = \sin(N_2 \Delta d\mathbf{q} \cdot \hat{x}'/2) / \sin(d\mathbf{q} \cdot \hat{x}'/2)$ and $M_2(N_2, \phi, \mathbf{q}) = \sin(N_2 d\mathbf{q} \cdot \hat{y}'/2) / \sin(d\mathbf{q} \cdot \hat{y}'/2)$ in Eq. (3) are conventional Fraunhofer diffraction patterns for an one-dimensional grating in mutually transverse direction. $\mu(\theta) = (1 + \cos\theta) \exp[-4k^2\beta^2 \sin^2(\theta/2)]$ is due to the gaussian aperture profile (Eq. (2)) modulated by a factor due to the absence of backscattering [2, 55] for MDFs in graphene, and $\mathbf{q} = \mathbf{k} - \mathbf{k}'$, $\mathbf{r}_n = n_1 d\hat{x}' + n_2 d\hat{y}'$, where n_1 and n_2 are integers, and the x', y' axis is rotated with respect to the incident electrons by an angle ϕ . For the first case, we take QDs arranged in square and hexagonal lattice arrangement with suitable choices of \mathbf{r}_n . The corresponding result, which is plotted in Fig. 1(b) in a polar plot, mimics the well-known Fraunhofer pattern with suitable modification due to the absence of back-scattering. This can be thought of as a two-dimensional generalisation of the well-known result of scattering by a smooth p-n junction in one dimension [1], $T \sim \exp(-\pi k_F \beta \sin^2(\theta)/2)$, as the scattering decreases exponentially with β in Eq. (3a) as $\frac{d\sigma}{d\theta} \sim e^{-4k^2\beta^2 \sin^2(\theta/2)}$ with a characteristic length(β in our case). In the inset of Fig. 1 (b), we show a polar plot of DSC from a single quantum dot. Due to Klein tunnelling, we can observe that the DSC is maximum in the forward direction and zero in the backward direction due to absence of backscattering [2, 55]. In Appendix B, we compare DSC of electrons scattered by TDQDL in non-relativistic two-

dimensional electron systems. In that case the absence of backscattering like the MDFs in Eq. (3) is absent. In case of MDFs in graphene the scattered MDFs are mostly confined in the forward direction [2, 55]. The comparison with the corresponding cases of non-relativistic charge carriers is discussed in Appendix B.

In the next two cases, we first consider a scattering lattice made of TDQDL with defects of different shapes and sizes (Eq. (3b), Fig. 2), and then a third case of scattering potential made with moiré pattern of two square lattices of TDQDL (Fig. 3), making the differential scattering cross-section dependent on the twist angle(δ) between the two square TDQDLs. The scattering amplitude for the TDQDL with a defect region is the difference between the contribution from the original TDQDL scattering potential (without the defect region) and a TDQDL of the same shape and position of the defect region in Eq. (3b). In the third case of moiré pattern, the scattering amplitude is again the sum of the contributions from two lattices rotated with respect to each other, and the differential scattering cross section in Eq. (3c) is the square of this sum. This happens due to the linearity property of the Fourier transform [36]. In the analogous case of optical diffraction systems, this is known as Babinet's principle [36, 63, 64].

For the square TDQDL with defect region, we have considered four specific cases by varying the locations and sizes of the cavities. For a square defect region ($(\Delta_d = 1)$) in a square TDQDL, the length of the side

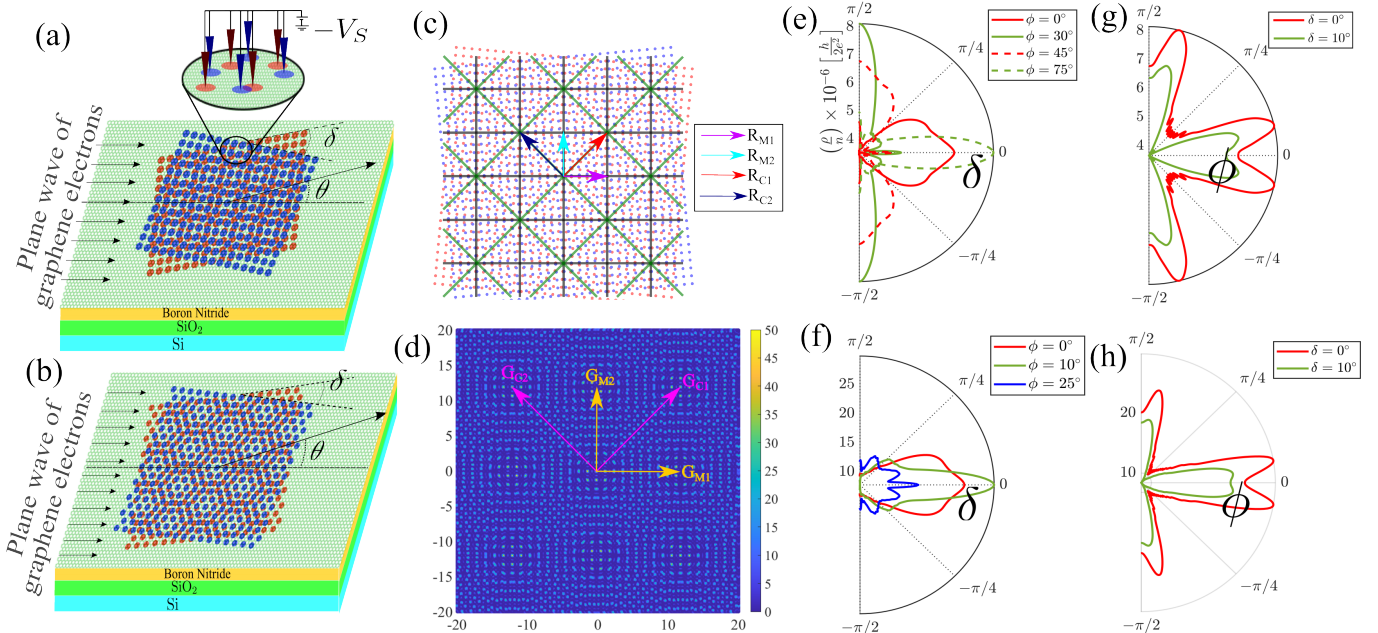


FIG. 3: The schematic diagram of a plane wave of massless Dirac fermions getting scattered by a moiré superlattice of two (a) square and (b) hexagonal lattices of Gaussian quantum dots(QD) in graphene. Moiré pattern made by two square lattices of TDQDL producing a commensurate structure at a twist angle, $\delta \approx 6.026^\circ$ is shown in (c). The moiré lattice is shown in green, and the commensurate lattice is shown in black. Such quantum dots can be created in experimental system by using tips with applied gate voltage in the same way as in Fig. 1. In (d) $|\tilde{V}(\mathbf{q}_1)|^2$ is plotted as a function of q_{1x} and q_{1y} for the above scattering potential. The resistivity pattern with fixed the mean angle(ϕ) is shown in (e) and (f) for a TDQDL scattering potential made with moiré pattern of two square and hexagonal lattices, respectively. In (g) and (h), the resistivity pattern is plotted with fixed twist angle(δ) again for a moiré pattern of two square and hexagonal lattices, respectively.

of the square-shaped cavities(N_{d2}) is varied to vary the size of the cavities. We have also taken two cases where the centre of the defect region does not coincide with the centre of the parent square TDQDL. For the moiré pattern, the moiré lattice vector d_M is related to the twist angle by $\delta = 2 \sin^{-1} \left(\frac{d}{2d_M} \right)$ [65]. The Bragg condition for the first two cases in Eq. (3a) and (3b) is given by $k^2 d^2 \sin^2 \left(\frac{\theta}{2} \right) = (n_1^2 + n_2^2) \pi^2$, where n_1 and n_2 are integers (see Fig. 8 in Appendix C).

The moiré pattern produces a periodic pattern with lattice periodicities $\sqrt{2N}d_M$ [65, 66] for the commensurate angles where N is an integer. The commensurate super-cell lattice vectors [67, 68] for $\phi = 0$ are given by $\mathbf{R}_{C1} = \left(\frac{d}{2 \sin(\delta/2)} \right) N(\hat{x} + \hat{y})$ and $\mathbf{R}_{C2} = \left(\frac{d}{2 \sin(\delta/2)} \right) N(-\hat{x} + \hat{y})$

For every value of N , we get a set of commensurate angles. For the particular commensurate structure that we have considered for square lattice, this common period is larger than the moiré cell by factor $\sqrt{2}$ [65] (see Fig. 3(c)). The moiré lattice with lattice periodicity d_M is shown in green. This commensurate lattice is shown in black in Fig. 3(c). The primitive lattice vectors

\mathbf{R}_{C1} and \mathbf{R}_{C2} are not same as the moiré lattice vectors $\mathbf{R}_{M1} = \left(\frac{d}{2 \sin(\delta/2)} \right) \hat{x}$ and $\mathbf{R}_{M2} = \left(\frac{d}{2 \sin(\delta/2)} \right) \hat{y}$. Due to the commensurate periodicity, scattering potentials made with such patterns show additional Bragg condition from Eq. (3c),

$$2Nk^2 d_M^2 \sin^2 \left(\frac{\theta}{2} \right) = (m_1^2 + m_2^2) \quad (4)$$

The detailed discussion on the maximum scattering conditions is shown in Appendix C.

To understand how the above results can be interpreted as an electronics analogue of Fourier optics in a succinct way, in the left column of TABLE I we list quantities that characterise a Fraunhofer diffraction-based spatial frequency filtering in optical imaging systems [32, 34, 35] and are demonstrated in Figs. 1 (e), (f), (g). In the right column of the same table, we list the corresponding quantities that define the analogue system of MDF scattered by a QD lattice. From TABLE I, we can observe that both the scattering amplitude in our system, $f(\theta)$ and the amplitude distribution at the spatial frequency plane in Fig. 1(e), $G(u, v)$ is the Fourier transform of the scattering potential $V(x', y')$ and the object distribution $g(x', y')$ respectively, whereas the presence

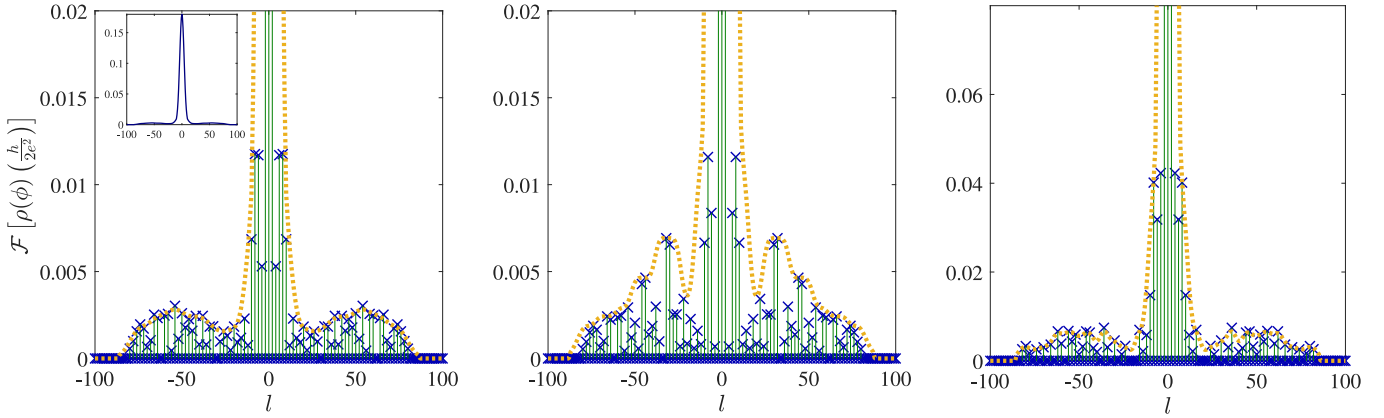


FIG. 4: (a) Shows the Fourier transform(FT) of the resistivity pattern for a TDQDL with $N_2 = 50$, $\Delta = 1$ and $d = 70\text{nm}$. The blue cross (\times) denotes the value of amplitude corresponding to each spatial frequency (l). In the inset, we have shown the total data. The main figures do not show the central peak to display the smaller values. The FT of the resistivity pattern through a Gaussian filter for the same TDQDL scattering potential with a square defect region (in the centre) is shown in (b). In (c), we show the FT of the resistivity pattern through a Gaussian filter for a scattering potential made with a moiré pattern of two square TDQDL with the same lattice constant.

of $(1 + e^{i\theta})$ term in $f(\theta)$ of MDF indicates the absence of backscattering [2, 5, 55]. For MDF, the position coordinate (\mathbf{r}) is transformed to angular wave number coordinate (\mathbf{q}), whereas in the corresponding optical system, the coordinates of the plane of aperture, x' and y' , are transformed to u and v , respectively. Correspondingly, the differential cross section, $\frac{d\sigma}{d\theta}$ in the case of MDF is replaced by intensity distribution I in the optical case as demonstrated in Figs. 1(b) and (f),

A noteworthy difference with the corresponding optical system appears when the superposition of two such TDQDL, rotated with respect to each other so that the resulting pattern is a moiré pattern, widely studied in optics [15, 69–71] and condensed matter [67, 68, 72–76]. Such moiré patterns are studied in optical imaging to improve the microscope's imaging capabilities in Structural Imaging Microscopy [77–79]. In optical systems, the resultant aperture profile for two transparencies $g_1(x', y')$ and $g_2(x', y')$ is $g_1(x', y') \times g_2(x', y')$ [80, 81]. This leads to a new pattern which consists of new beating frequencies [82]. However, for MDF scattered by two potentials $V_1(x', y')$ and $V_2(x', y')$, the differential scattering cross-section depends on the Fourier transform of $V_1(x', y') + V_2(x', y')$. This leads to additional maximum scattering conditions from Eq. (3c) as shown in Eq. (4) and depicted in Fig. 3 (d). The resultant scattering potential shows a new periodicity only for commensurate angles.

The above analogy between the scattering problem of MDF from TDQDL and the Fourier optics using a 2D grating naturally leads to the question if this can be extended to the electronic analogue of optical image processing. In optical systems this is achieved through a second FT through lenses in the optical system (see Fig. 1(g)). In our system, we introduce another degree of freedom, by rotating our scattering potential

about a transverse axis passing through the centre of the TDQDL. We define a spatial angle ϕ between the propagation direction of the MDF and the symmetry axis of the TDQDL in the graphene plane. While a direct analogy with the optical image processing is difficult, we show that some information about the structure of the TDQDL can be retrieved by calculating the dc resistivity at zero temperature for different rotation angles (ϕ). Using the semiclassical Boltzmann theory, the dc resistivity at zero temperature [83, 84] is given by

$$\rho = \frac{2n v_F \sigma_{tr}}{e^2 v_F^2 D(E_F)} = \frac{2n}{e^2 v_F D(E_F)} \int_0^{2\pi} d\theta (1 - \cos \theta) \frac{d\sigma}{d\theta}. \quad (5)$$

We note that Eq. (5) is valid in the limit of small concentration (n) of scattering centers due to quantum dot lattice potential. Here, e = charge of an electron, v_F = Fermi velocity, $D(E_F)$ = density of states at Fermi energy (variation of resistivity with E_F is discussed in Fig. 9 of Appendix D) and σ_{tr} is the transport scattering cross-section. Corresponding values of the resistivities in systems considered are within the typical range of observed resistivities in graphene-based systems [86, 87, 92]. Additionally, our calculated values of resistivities can also be adjusted by choosing the gate voltages applied at every QD and varying the height of the scatterers.

The corresponding results, namely the angular distribution of resistivity, are plotted in Figs. 1(c) and (d) for square and hexagonal TDQDL, in Figs. 2(a) and (b) for TDQDL with a defect region , and in Figs. 3 (e),(f),(g) and (h) for moiré pattern of two TDQDL lattices, to demonstrate how certain structural information of these TDQDLs can be retrieved from this angle-resolved resistivity.

We begin with the observation that $\rho(\phi)$ in Figs. 1(c) and (d) reflects the discrete rotational symmetry of

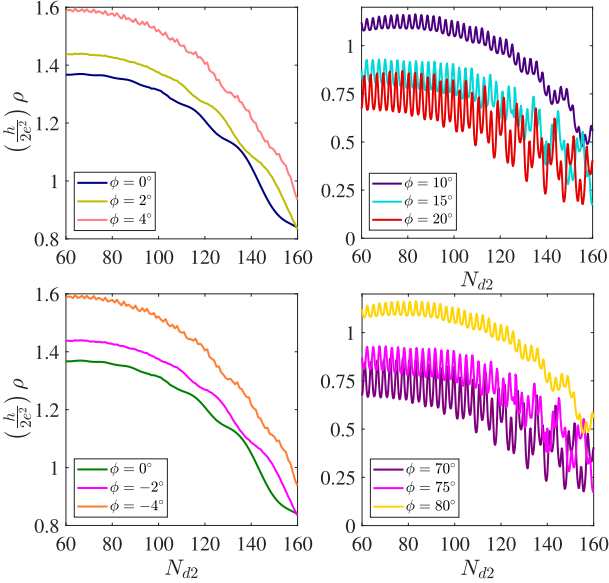


FIG. 5: Resistivity vs N_{d2} plot for different values of ϕ .

the square and hexagonal lattice, e.g. $\left. \frac{d\sigma}{d\theta} \right|_{\Delta, N_2, \phi=0^\circ} = \left. \frac{d\sigma}{d\theta} \right|_{\frac{1}{\Delta}, \Delta N_2, \phi=90^\circ}$ in case for square lattice, but not for the hexagonal lattice. This may be contrasted with the observation in Figs. 1(c) and (d) that $\rho(-\pi/2) = \rho(\pi/2)$ for both square and hexagonal lattice of TDQDL. For TDQDL with a defect region, the resistivity pattern calculated with the help of Eq. (3b) and Eq. (5) reveals both the symmetry of the TDQDL, as well as the location and size of the defect region. In Fig. 2(a) comparing between blue, red, and orange-yellow plots of the $\rho(\phi)$, we see that the location of the square defect region in the corresponding square TDQDL indeed exhibits itself in the symmetry of the resistivity plot about the $\phi = 0$ line. Similarly, comparing the cases of orange-yellow and the green plots of $\rho(\phi)$, we see that the size of the defect region, which is proportional to the number of removed scattering centres, indeed affects the magnitude of the resistivity pattern. Hexagonal TDQDL, with cavities of circular shape with radius(r_d) in Fig. 2(b), shows the same effect (see Appendix E). In Fig. 5, we show the dependence on resistivity at different values of ϕ on the size of the defect region. From Fig. 5, we can observe that the plot is the same for angles ϕ , $(\pi/2 - \phi)$ and $-\phi$. As both the original scattering lattice is made of square lattice and of square shape($\Delta = 1$) and the defect region is also in the shape of a square, this symmetry comes.

The differential scattering cross section for the scattering potential made with a moiré pattern of two square lattices of TDQDL is shown in Eq. (3c). In Fig. 3 (d), we show $\tilde{V}(\mathbf{q})$ as a function of q_{1x} and q_{1y} (see Appendix C). As expected, FT is also a moiré pattern of two square patterns in inverse space but multiplied by the same $\mu(\theta)$ given in Eq. (3c). In Fig. 3, (e), we show the dependence of the resistivity pattern on the twist angle(δ) for fixed

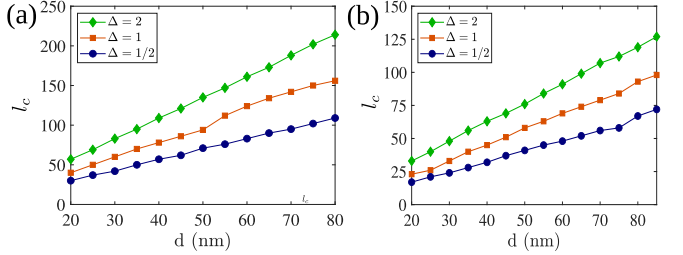


FIG. 6: Cut-off frequency(l_c) vs lattice constant(d) plot in the case for (a) square and TDQDL with $N_2 = 100$ (b) hexagonal TDQDL with $N_2 = 30$.

values of average angle (ϕ) with the incident plane wave of massless Dirac fermions.

The most prominent features of these resistivity plots of TDQDL in Figs. 1(c) and (d), for TDQDL with cavities in Figs. 2(a), and (b), and for moiré pattern of TDQDLs in Figs. 3(e)-(h), are oscillations in resistivity as a function of the angular variable (see Appendix F). To understand the oscillations (see Appendix G) in resistivity plots Figs. 1(c) and (d) in a more quantitative way we did an FT of the resistivity that can provide the range of these angular frequencies (see Fig. 4). If we choose l as the conjugate variable of ϕ , we can denote the highest angular frequency component present in one ρ vs ϕ curve as l_c or cut-off angular frequency for a given lattice.

For the single layer of TDQDL, l_c depends on the lattice parameter of the scattering lattice as the DSC also depends on the lattice parameter in Eq. (3a). In Fig. 6, we show the dependence of cut-off frequency on the lattice constant both for square and hexagonal lattice. Here, we see that at a particular value of d , the cut-off frequency is different for different Δ values. In Fig. 4 (a), the Fourier spectrum of the resistivity pattern as a function of l for a TDQDL shows a feature that is similar to the side-band formation. We highlight this aspect through an envelope function (dotted orange curve) over the actual result. For the same TDQDL, with a defect region at the centre, and for the same cut-off frequency, this side-band like feature becomes more prominent in Fig. 4 (b), whereas this side-band like feature gets highly suppressed in the case of moiré pattern of two relatively twisted TDQDLs in Fig. 4 (c). These points out that certain angular frequency components get enhanced or suppressed as the scattering region is removed or added, a phenomenon akin to the spatial frequency filtering in Fourier optics, but now happening in the solid state environment for the angle-resolved resistivity, a transport coefficient. This can also be linked to the electronic analogue of Babinet's principle that we reported earlier in this manuscript. In the ballistic transport regime, the spatial frequency filtering in the angle resolved resistivity of MDFs scattered from TDQDL is shown as an electronic analogue of Babinet's principle. This forms one of the most prominent findings in this work.

III. DISCUSSION

To summarize, using the Lippmann-Schwinger formalism, we established an electronic analogue of Fourier optics i.e., FEO by mapping the scattering cross-section of MDF from TDQDLs to the Fraunhofer diffraction pattern and providing a dictionary of such mapping. By considering TDQDL with defect region and moiré pattern of such TDQDLs, we demonstrated an electronic analogue of Babinet's principle. Harnessing this analogy further with an eye on practical application, we evaluated the angle-resolved resistivity of these scattered MDs, and Fourier analyze the same to show that the Fourier spectrum shows spatial frequency filtering consistent with Babinet's principle. With the quantum dot arrays now routinely produced in semiconductor-based systems [59–61], we hope our proposed analogy can be used for making new electronic devices based on such analogue FEO.

IV. ACKNOWLEDGMENT

We thank Kedar Khare, Rohit Narula and Deepanshu Aggarwal for the helpful discussions. SG and RM are supported by a SPARC Phase II (MHRD, GOI, Project Code P2117) grant, whereas PSB is supported by a MHRD Fellowship.

V. DATA AVAILABILITY STATEMENT

All data that support the findings of this work is included in the main manuscript and supplementary file.

VI. CONFLICT OF INTEREST

There is also no competing interest between the authors.

Appendix A: Lippmann-Schwinger Integral Equation and Transition Operator

In the presence of a scattering potential $V(\mathbf{r})$, the scattered wavefunction for MDF can be written using the Lippmann-Schwinger formalism [57, 58] as,

$$\Psi_{\mathbf{k}}^{\eta, \pm}(\mathbf{r}) = \phi_{\mathbf{k}}^{\eta}(\mathbf{r}) + \int d^2 \mathbf{r}' G_0^{\pm}(\mathbf{r}, \mathbf{r}', E) V(\mathbf{r}') \Psi_{\mathbf{k}}^{\eta, \pm}(\mathbf{r}') \quad (\text{A1})$$

The Green's function for the physically relevant outgoing wave case for MDF is given by,

$$G_0^+(\mathbf{r}, \mathbf{r}', E) = -\frac{1}{\hbar v_F} \sqrt{\frac{ik}{8\pi r}} e^{ikr} e^{-i\mathbf{k}' \cdot \mathbf{r}'} \begin{bmatrix} 1 & e^{-i\theta} \\ e^{i\theta} & 1 \end{bmatrix} \quad (\text{A2})$$

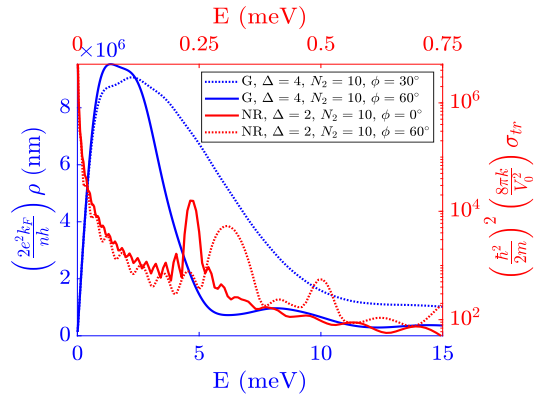


FIG. 7: The energy dependence of the resistivity for graphene(G) and non-relativistic(NR) two dimensional systems.

In the case of First Born Approximation(FBA), the transition operator is approximated till the first term. Which makes the scattering amplitude

$$f^{(1)} = -\frac{1}{2\hbar v_F} \sqrt{\frac{ik}{2\pi}} (1 + e^{-i\theta}) \tilde{V}(\mathbf{k} - \mathbf{k}'). \quad (\text{A3})$$

The asymptotic scattered wave function is given by

$$\Psi_{\mathbf{k}}^{e,+}(\mathbf{r}) = \phi_{\mathbf{k}}^e(\mathbf{r}) + \frac{1}{\sqrt{2}} \begin{bmatrix} 1 \\ e^{i\theta} \end{bmatrix} \frac{e^{ikr}}{\sqrt{r}} f(\theta) \quad (\text{A4})$$

Appendix B: Differernce between Scattering of 2DES and Graphene Electrons

The differential scattering cross sections for electrons in a two-dimensional electron system(2DES) scattered from a square TDQDL is given by

$$\frac{d\sigma}{d\theta} = \left(\frac{2m}{\hbar^2} \right)^2 \left(\frac{V_0^2}{8\pi k} \right) e^{-4k^2 \beta^2 \sin^2(\frac{\theta}{2})} M_1^2(\theta, \phi) M_2^2(\theta, \phi). \quad (\text{B1})$$

By comparing Eq. (3a) (main text) and (B1), we can observe that the differential scattering cross section in graphene is proportional to $k(\sim E)$, but in 2DES, it is proportional to $1/k (\sim E^{-1/2})$ [88–90]. This difference of energy dependence can be understood from Fig. 7, where we show the transport scattering cross section for massless Dirac fermions both in the case of graphene and two-dimensional non-relativistic systems. We can observe from Eq. (3a) that for scattering at low energy, the differential scattering cross section for massless-Dirac fermions becomes $\frac{d\sigma}{d\theta} = \frac{k\Delta^2 N_2^4 V_0^2}{4\pi\hbar^2 v_F^2} (1 + \cos\theta)$. That makes the transport scattering cross section $\sigma_{tr} = \left(\frac{\Delta^2 N_2^4 V_0^2}{4\hbar^2 v_F^2} \right) k$ and the resistivity becomes, $\rho = \left(\frac{n\pi^2 \Delta^2 N_2^4 V_0^2}{2\hbar e^2 k_F v_F^2} \right) k$. Due to

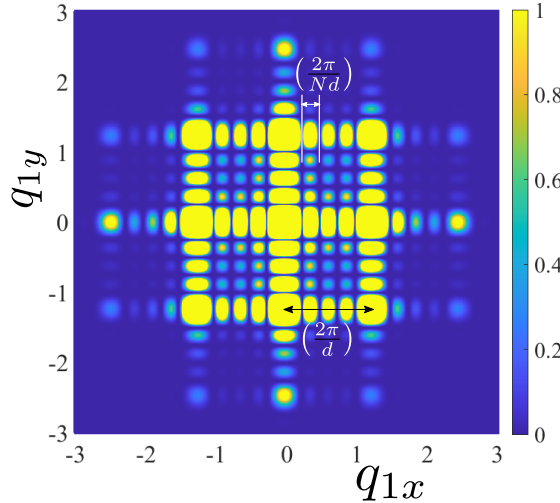


FIG. 8: $|\tilde{V}(\mathbf{q})|^2$ plotted as a function of q_{1x} and q_{1y} for a single layer of TDQDL for $N = 5$.

this, we see the linear variation of resistivity with E at low energies in Fig. 7. From Eq. (B1) for non-relativistic electrons in 2D, at low energy the differential scattering cross section becomes, $\frac{d\sigma}{d\theta} = \left(\frac{2m}{\hbar^2}\right)^2 \left(\frac{V_0^2}{8\pi k}\right) \Delta^2 N_2^4$. The transport scattering cross section becomes $\sigma_{tr} = \left(\frac{mV_0\Delta N_2^2}{\hbar^2}\right)^2 \times \frac{1}{k}$. In Fig. 7, we see that at low energies, the transport scattering cross section becomes inversely proportional to the energy of the incident particle.

Appendix C: Condition for Maximum Scattering in case of moiré pattern of two TDQDL

The differential scattering cross-section for these systems is directly proportional to $|\tilde{V}(\mathbf{q})|^2$. Here $\tilde{V}(\mathbf{q})$ is the Fourier transform of the scattering potential $V(\mathbf{r})$. In Fig. 8, we show the Fourier transform of the scattering potential made by a square TDQDL. The positions for the principle maximas are given by $q_{1x} = n_1(2\pi/d)$ and $q_{1y} = n_2(2\pi/d)$ where n_1 and n_2 are integers. These correspond to the Bragg condition. The secondary minimas are separated by a distance of $(\frac{2\pi}{Nd})$. We can also notice that $|\tilde{V}(\mathbf{q})|^2$ has maximum value for the central maxima at $q_{1x} = 0$ and $q_{1y} = 0$ because the Fourier transform of the scattering potential has a Gaussian term $e^{-4k^2\beta^2 \sin^2(\theta/2)}$ same as in $\mu(\theta)$ in Eq. (3a) (main text).

For the case of moiré pattern of two square TDQDL scattering potentials, we have shown the maximum scattering cases in Fig. 3 (d) (main text). We can observe that the Fourier transform is also a moiré pattern of two square patterns in inverse space. The reciprocal lattice vectors, in this case, is

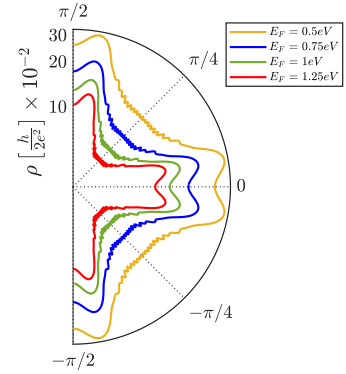


FIG. 9: The resistivity pattern for different values of E_F at $N_2 = 100$ and $\Delta = 1$.

$$\mathbf{G}_{\mathbf{M1}} = \frac{4\pi \sin(\frac{\delta}{2})}{d} \hat{x}, \quad \mathbf{G}_{\mathbf{M2}} = \frac{4\pi \sin(\frac{\delta}{2})}{d} \hat{y} \quad (\text{C1})$$

$$\mathbf{G}_{\mathbf{C1}} = \frac{4\pi \sin(\frac{\delta}{2})}{d} N(\hat{x} + \hat{y}), \quad \mathbf{G}_{\mathbf{C2}} = \frac{4\pi \sin(\frac{\delta}{2})}{d} N(\hat{y} - \hat{x}) \quad (\text{C2})$$

Where, N is an integer. For every value of N , we have a set of commensurate angles.

The Fourier transform produces a commensurate pattern only when the scattering potential itself produces a commensurate pattern. The Bragg conditions, which appear only in the case of commensurate lattice i.e., Eq. (4) correspond to those points in Fig. 3 (d) for which $\mathbf{q} = m_1 \mathbf{G}_{\mathbf{C1}} + m_2 \mathbf{G}_{\mathbf{C2}}$.

Appendix D: Dependence of Resistivity Pattern on Fermi Energy

For monolayer graphene systems, the fermi energy (E_F) and the fermi momentum are controlled by a back-gate voltage V_g . If the back gate and the graphene layer are separated by a substrate of SiO_2 with a width of about 300nm, the Fermi momentum is given by [84],

$$k_F^2 = \pi \alpha V_g \quad (\text{D1})$$

where, $\alpha = 7.2 \times 10^{-4} \text{ V}^{-1} \text{ nm}^{-2}$. For a back-gate voltage of 100 V, the Fermi energy is 0.31 eV.

In Fig. 9, we show the resistivity pattern for different values of E_F for a fixed configuration. We can observe from here that the value of resistivity decreases with a larger value of Fermi energy [91–93].

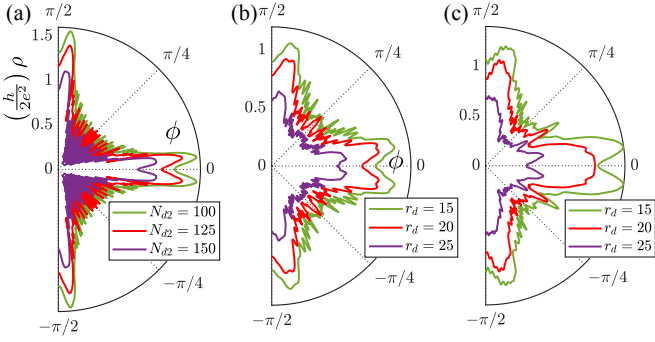


FIG. 10: Resistivity pattern for a TDQDL potential with (a) square defect region in a square TDQDL, (b) circular defect region in a square TDQDL and (c) circular defect region in a hexagonal TDQDL. We have compared defect regions of different sizes.

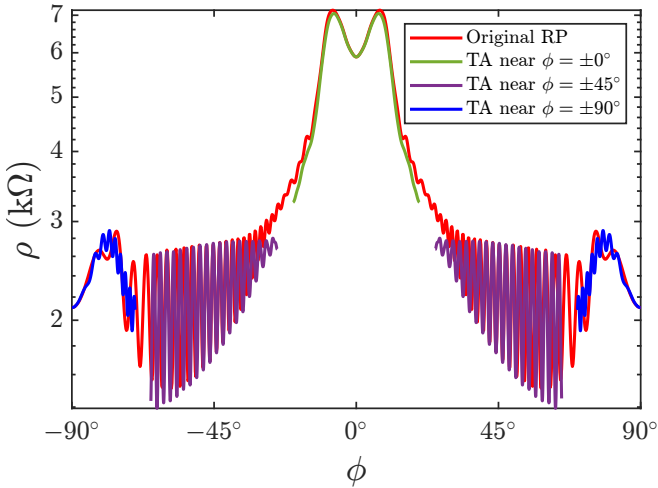


FIG. 11: Resistivity pattern for a TDQDL of dimension $N_2 = 50$ and $\Delta = 2$. The red plot shows the resistivity pattern (RP) calculated from Eq. (3a), the general ϕ dependent differential scattering cross-section. The green, magenta and blue plot shows the approximate value of resistivity near the values of $\phi = 0, \pm\frac{\pi}{4}$ and $\pm\frac{\pi}{2}$ using Taylor Approximation(TA).

Appendix E: Dependence of Resistivity Pattern on the Shape of Defect Region in the Scattering TDQDL Potential.

Here, we compare the resistivity pattern for TDQDL of different shapes in Fig. 10. To distinguish the shapes of defect regions, we have to check the symmetries of the

original lattice and the defect region.

In Fig. 10, we can observe that the resistivity pattern depends on the size of the defect region. Now, we can choose a fixed rotation value ϕ and compare the resistivity values for different values of N_{d2} .

Appendix F: Approximations of Resistivity Pattern at Various ϕ values for Single Layer of TDQDL

The resistivity plots in Figs. 1(c) and (d) (main text) as a function of ϕ show oscillations having different amplitudes around different angles. To understand them, near $\phi = 0, \pm\frac{\pi}{4}, \pm\frac{\pi}{2}$ we evaluate the resistivity with a Taylor expansion around each of these angles, and corresponding approximate plots are then superposed with the exact one evaluated with Eq. (5) in Fig. 11, for a square TDQDL calculated for $N_2 = 50$ and $\Delta = 2$. As expected, they almost overlap near each angle over a range and start showing deviation as one sifts from these angles.

Appendix G: Oscillations in the Resistivity Pattern

We observe from Figs. 1 (c) and (d) (main text) that the frequency of oscillations in the ρ vs ϕ plot increases with a higher value of Δ for a fixed N_2 . To explain this, note that the only term in Eq. (3a) (main text) that depends on Δ is $\sin^2(N_2\Delta kd\sin(\frac{\theta}{2})\sin(\frac{\theta}{2} - \phi))$. It has a period(in ϕ) of oscillation $l_P = \sin^{-1}\left[\frac{\pi}{N_2\Delta kd\sin(\frac{\theta}{2})}\right]$.

Hence, the frequency of oscillation in the resistivity pattern is higher for a higher value of Δ .

Moiré Pattern of Two QD Scattering Lattices: As the moiré pattern produced by two square lattices with $\delta = \Delta\delta$ and $\phi = 45^\circ$ is the same as the moiré pattern of $\delta = 90^\circ + \Delta\delta$ and $\phi = 45^\circ$, in the resistivity pattern of Fig. 3 (e) we observe that $\rho(\phi, \delta) = \rho(\phi \pm \frac{\pi}{4}, \delta \pm \frac{\pi}{2})$. The differential scattering cross section for these two cases is also the same, shown from Eq. (3c) (main text). Such symmetry is absent in the resistivity of moiré pattern of two hexagonal TDQDL lattices when plotted as a function of the twist angle (δ) in Fig. 3(f) (main text). Similarly, we observe whereas in Fig. 3(g) (main text) $\rho(\phi = 0^\circ, \delta) = \rho(\phi = 90^\circ, \delta)$ due to symmetry of the square lattice, this is not the case for the hexagonal counterpart in Fig. 3(h). As the moiré lattice vector is larger than the lattice vector of the original lattices, the spatial frequencies corresponding to moiré lattice vector are smaller than the spatial frequency corresponding to the lattice vector of the original lattice. Due to this, the same cut-off frequency analysis which was used for the earlier case in Fig. 6 can not detect the dependence of the cut-off on the moiré lattice vector.

[1] V. V. Cheianov and V. I. Fal'ko, Selective transmission of dirac electrons and ballistic magnetoresistance of $n-p$

junctions in graphene, *Phys. Rev. B* **74**, 041403 (2006).
[2] M. Katsnelson, K. Novoselov, and A. Geim, Chiral tun-

neling and the klein paradox in graphene, *Nat. Phys.* **2**, 620 (2006).

[3] V. V. Cheianov, V. Fal'ko, and B. L. Altshuler, The focusing of electron flow and a veselago lens in graphene *p-n* junctions, *Science* **315**, 1252 (2007).

[4] A. F. Young and P. Kim, Quantum interference and klein tunnelling in graphene heterojunctions, *Nature Phys* **5**, 222 (2009).

[5] N. Stander, B. Huard, and D. Goldhaber-Gordon, Evidence for klein tunneling in graphene *p-n* junctions, *Phys. Rev. Lett.* **102**, 026807 (2009).

[6] S. Chen, Z. Han, M. M. Elahi, K. M. M. Habib, L. Wang, B. Wen, Y. Gao, T. Taniguchi, K. Watanabe, J. Hone, A. W. Ghosh, and C. R. Dean, Electron optics with p-n junctions in ballistic graphene, *Science* **353**, 1522 (2016).

[7] J. B. Pendry, Negative refraction makes a perfect lens, *Phys. Rev. Lett.* **85**, 3966 (2000).

[8] D. Schurig, J. J. Mock, B. J. Justice, S. A. Cummer, J. B. Pendry, A. F. Starr, and D. R. Smith, Metamaterial electromagnetic cloak at microwave frequencies, *Science* **314**, 977 (2006).

[9] G.-H. Lee, G.-H. Park, and H.-J. Lee, Observation of negative refraction of dirac fermions in graphene, *Nat. Phys.* **11**, 925 (2015).

[10] B. Brun, N. Moreau, S. Somanchi, V.-H. Nguyen, K. Watanabe, T. Taniguchi, J.-C. Charlier, C. Stampfer, and B. Hackens, Imaging dirac fermions flow through a circular veselago lens, *Phys. Rev. B* **100**, 041401 (2019).

[11] S. Tchoumakov, J. Cayssol, and A. G. Grushin, Three-dimensional chiral veselago lensing, *Phys. Rev. B* **105**, 075309 (2022).

[12] X. Zhang, W. Ren, E. Bell, Z. Zhu, K.-T. Tsai, Y. Luo, K. Watanabe, T. Taniguchi, E. Kaxiras, M. Luskin, *et al.*, Gate-tunable veselago interference in a bipolar graphene microcavity, *Nat Commun* **13**, 6711 (2022).

[13] P. Bøggild, J. M. Caridad, C. Stampfer, G. Calogero, N. R. Papier, and M. Brandbyge, A two-dimensional dirac fermion microscope, *Nat. Commun* **8**, 15783 (2017).

[14] C.-H. Park, Y.-W. Son, L. Yang, M. L. Cohen, and S. G. Louie, Electron beam supercollimation in graphene superlattices, *Nano Letters* **8**, 2920 (2008).

[15] M.-H. Liu, C. Gorini, and K. Richter, Creating and steering highly directional electron beams in graphene, *Phys. Rev. Lett.* **118**, 066801 (2017).

[16] K. Wang, M. M. Elahi, L. Wang, K. M. Habib, T. Taniguchi, K. Watanabe, J. Hone, A. W. Ghosh, G.-H. Lee, and P. Kim, Graphene transistor based on tunable dirac fermion optics, *Proc. Natl. Acad. Sci. U.S.A.* **116**, 6575 (2019).

[17] D. S. Wei, T. van der Sar, J. D. Sanchez-Yamagishi, K. Watanabe, T. Taniguchi, P. Jarillo-Herrero, B. I. Halperin, and A. Yacoby, Mach-zehnder interferometry using spin-and valley-polarized quantum hall edge states in graphene, *Sci. Adv.* **3**, e1700600 (2017).

[18] M. Jo, P. Brasseur, A. Assouline, G. Fleury, H.-S. Sim, K. Watanabe, T. Taniguchi, W. Dummerpnach, P. Roche, D. C. Glattli, N. Kumada, F. D. Parmentier, and P. Roulleau, Quantum hall valley splitters and a tunable mach-zehnder interferometer in graphene, *Phys. Rev. Lett.* **126**, 146803 (2021).

[19] P. Rickhaus, R. Maurand, M.-H. Liu, M. Weiss, K. Richter, and C. Schönenberger, Ballistic interferences in suspended graphene, *Nat. Commun.* **4**, 2342 (2013).

[20] G. Forghieri, P. Bordone, and A. Bertoni, Time-dependent transport in graphene mach-zender interferometers, *Phys. Rev. B* **106**, 165402 (2022).

[21] P. Rickhaus, P. Makk, M.-H. Liu, K. Richter, and C. Schönenberger, Gate tuneable beamsplitter in ballistic graphene, *Appl. Phys. Lett.* **107**, 251901 (2015).

[22] C. Handschin, P. Makk, P. Rickhaus, M.-H. Liu, K. Watanabe, T. Taniguchi, K. Richter, and C. Schönenberger, Fabry-pérot resonances in a graphene/hbn moiré superlattice, *Nano Lett.* **17**, 328 (2017).

[23] E. Paredes-Rocha, Y. Betancur-Ocampo, N. Szpak, and T. Stegmann, Gradient-index electron optics in graphene *p-n* junctions, *Phys. Rev. B* **103**, 045404 (2021).

[24] R. L. Heinisch, F. X. Bronold, and H. Fehske, Mie scattering analog in graphene: Lensing, particle confinement, and depletion of klein tunneling, *Phys. Rev. B* **87**, 155409 (2013).

[25] R. N. Sajjad, S. Sutar, J. U. Lee, and A. W. Ghosh, Manifestation of chiral tunneling at a tilted graphene *p-n* junction, *Phys. Rev. B* **86**, 155412 (2012).

[26] F. Anwar, A. Iurov, D. Huang, G. Gumbs, and A. Sharma, Interplay between effects of barrier tilting and scatterers within a barrier on tunneling transport of dirac electrons in graphene, *Phys. Rev. B* **101**, 115424 (2020).

[27] S. Ghosh and M. Sharma, Electron optics with magnetic vector potential barriers in graphene, *J. Phys.: Condens. Matter* **21**, 292204 (2009).

[28] M. Sharma and S. Ghosh, Electron transport and goos-hänchen shift in graphene with electric and magnetic barriers: optical analogy and band structure, *J. Phys.: Condens. Matter* **23**, 055501 (2011).

[29] Y. Zhao, A. Leuch, O. Zilberberg, and A. Štrkalj, Electron optics using negative refraction in two-dimensional inverted-band *pn* junctions, *Phys. Rev. B* **108**, 195301 (2023).

[30] M. Karalic, A. Štrkalj, M. Masseroni, W. Chen, C. Mittag, T. Tschirky, W. Wegscheider, T. Ihn, K. Ensslin, and O. Zilberberg, Electron-hole interference in an inverted-band semiconductor bilayer, *Phys. Rev. X* **10**, 031007 (2020).

[31] P. M. Duffieux, *L'intégrale de Fourier et ses applications à l'optique*, Imprimeries Oberthur, Rennes, France, (1946); English version: P. M. Duffieux, *The Fourier Transform and Its Applications to Optics*, (Wiley, 1983).

[32] K. Birch, A spatial frequency filter to remove zero frequency, *Opt. Acta* **15**, 113 (1968).

[33] A. Ghatak, *Optics* (Tata McGraw-Hill Publishing Company Limited, 2009).

[34] J. Goodman, *Introduction to Fourier Optics*, McGraw-Hill physical and quantum electronics series (W. H. Freeman, 2005).

[35] K. G. Birch, Spatial filtering in optical data-processing, *Rep. Prog. Phys.* **35**, 1265 (1972).

[36] M. Born and E. Wolf, *Principles of Optics: Electromagnetic Theory of Propagation, Interference and Diffraction of Light (7th Edition)*, 7th ed. (Cambridge University Press, 1999).

[37] F. Jenkins and H. White, *Fundamentals of Optics*, International student edition (McGraw-Hill, 1976).

[38] P. Silvestrov and K. Efetov, Quantum dots in graphene, *Phys. Rev. Lett.* **98**, 016802 (2007).

[39] D. Joung, L. Zhai, and S. I. Khondaker, Coulomb blockade and hopping conduction in graphene quantum dots array, *Phys. Rev. B* **83**, 115323 (2011).

[40] F. Ghahari, D. Walkup, C. Gutiérrez, J. F. Rodriguez-Nieva, Y. Zhao, J. Wyrick, F. D. Natterer, W. G. Cullen, K. Watanabe, T. Taniguchi, L. S. Levitov, N. B. Zhitenev, and J. A. Stroscio, An on/off berry phase switch in circular graphene resonators, *Science* **356**, 845 (2017).

[41] C. Gutiérrez, D. Walkup, F. Ghahari, C. Lewandowski, J. F. Rodriguez-Nieva, K. Watanabe, T. Taniguchi, L. S. Levitov, N. B. Zhitenev, and J. A. Stroscio, Interaction-driven quantum hall wedding cake like structures in graphene quantum dots, *Science* **361**, 789 (2018).

[42] H. V. Grushevskaya, G. G. Krylov, S. P. Kruchinin, B. Vlahovic, and S. Bellucci, Electronic properties and quasi-zero-energy states of graphene quantum dots, *Phys. Rev. B* **103**, 235102 (2021).

[43] J. Lee, D. Wong, J. Velasco Jr, J. F. Rodriguez-Nieva, S. Kahn, H.-Z. Tsai, T. Taniguchi, K. Watanabe, A. Zettl, F. Wang, *et al.*, Imaging electrostatically confined dirac fermions in graphene quantum dots, *Nature Phys.* **12**, 1032 (2016).

[44] Y. Zhao, J. Wyrick, F. D. Natterer, J. F. Rodriguez-Nieva, C. Lewandowski, K. Watanabe, T. Taniguchi, L. S. Levitov, N. B. Zhitenev, and J. A. Stroscio, Creating and probing electron whispering-gallery modes in graphene, *Science* **348**, 672 (2015).

[45] R. Zhao, P. Wan, L. Zhou, D. Huang, H. Guo, H. Xia, and J. Du, Electron metasurfaces in graphene, *Phys. Rev. B* **107**, 155404 (2023).

[46] Y. Ren, Y. Gao, P. Wan, Q. Wang, D. Huang, and J. Du, Effective medium theory for electron waves in a gate-defined quantum dot array in graphene, *Phys. Rev. B* **100**, 045422 (2019).

[47] Y. Tang, X. Cao, R. Guo, Y. Zhang, Z. Che, F. T. Yannick, W. Zhang, and J. Du, Flat-lens focusing of electron beams in graphene, *Scientific Reports* **6**, 33522 (2016).

[48] S.-Y. Li and L. He, Recent progresses of quantum confinement in graphene quantum dots, *Front. Phys.* **17**, 1 (2022).

[49] K. S. Novoselov, A. K. Geim, S. V. Morozov, D. Jiang, Y. Zhang, S. V. Dubonos, I. V. Grigorieva, and A. A. Firsov, Electric field effect in atomically thin carbon films, *Science* **306**, 666 (2004).

[50] A. C. Neto, F. Guinea, N. M. Peres, K. S. Novoselov, and A. K. Geim, The electronic properties of graphene, *Rev. Mod. Phys.* **81**, 109 (2009).

[51] S. Bhandari, G. H. Lee, K. Watanabe, T. Taniguchi, P. Kim, and R. M. Westervelt, Imaging electron flow from collimating contacts in graphene, *2D Mater.* **5**, 021003 (2018).

[52] C. Gutiérrez, L. Brown, C.-J. Kim, J. Park, and A. N. Pasupathy, Klein tunnelling and electron trapping in nanometre-scale graphene quantum dots, *Nat. Phys.* **12**, 1069 (2016).

[53] S. Bhandari, G.-H. Lee, A. Klales, K. Watanabe, T. Taniguchi, E. Heller, P. Kim, and R. M. Westervelt, Imaging cyclotron orbits of electrons in graphene, *Nano Lett.* **16**, 1690 (2016).

[54] J. Berezovsky and R. M. Westervelt, Imaging coherent transport in graphene (part ii): probing weak localization, *Nanotechnology* **21**, 274014 (2010).

[55] P. E. Allain and J.-N. Fuchs, Klein tunneling in graphene: optics with massless electrons, *Eur. Phys. J. B* **83**, 301 (2011).

[56] C. Dartora, F. Zanella, and G. Cabrera, The theory for a 2d electron diffractometer using graphene, *J. Appl. Phys.* **132**, 124305 (2022).

[57] J. J. Sakurai, *Modern quantum mechanics*, rev. ed ed. (Addison-Wesley Pub. Co, 1994).

[58] S. K. Adhikari, Quantum scattering in two dimensions, *Am. J. Phys.* **54**, 362 (1986).

[59] X. Wang, E. Khatami, F. Fei, J. Wyrick, P. Namboodiri, R. Kashid, A. F. Rigos, G. Bryant, and R. Silver, Experimental realization of an extended fermi-hubbard model using a 2d lattice of dopant-based quantum dots, *Nat Commun* **13**, 6824 (2022).

[60] D. Schröer, A. D. Greentree, L. Gaudreau, K. Eberl, L. C. L. Hollenberg, J. P. Kotthaus, and S. Ludwig, Electrostatically defined serial triple quantum dot charged with few electrons, *Phys. Rev. B* **76**, 075306 (2007).

[61] T. Hensgens, T. Fujita, L. Janssen, X. Li, C. Van Diepen, C. Reichl, W. Wegscheider, S. Das Sarma, and L. M. Vandersypen, Quantum simulation of a fermi-hubbard model using a semiconductor quantum dot array, *Nature* **548**, 70 (2017).

[62] J. Salfi, J. Mol, R. Rahman, G. Klimeck, M. Simmons, L. Hollenberg, and S. Rogge, Quantum simulation of the hubbard model with dopant atoms in silicon, *Nat Commun* **7**, 11342 (2016).

[63] J. Babinet, *C.R. Acad. Sci.* , Vol. 4 (1837), 638.

[64] J. R. Jiménez and E. Hita, Babinet's principle in scalar theory of diffraction, *Opt. Rev.* **8**, 495 (2001).

[65] A. Dunbrack and J. Cano, Intrinsically multilayer moiré heterostructures, *Phys. Rev. B* **107**, 235425 (2023).

[66] O. Can, T. Tummuru, R. P. Day, I. Elfimov, A. Damascelli, and M. Franz, High-temperature topological superconductivity in twisted double-layer copper oxides, *Nat. Phys.* **17**, 519 (2021).

[67] J. M. B. Lopes dos Santos, N. M. R. Peres, and A. H. Castro Neto, Graphene bilayer with a twist: Electronic structure, *Phys. Rev. Lett.* **99**, 256802 (2007).

[68] S. Carr, S. Fang, and E. Kaxiras, Electronic-structure methods for twisted moiré layers, *Nat. Rev. Mater.* **5**, 748 (2020).

[69] R. Bracewell, *Two-dimensional Imaging*, Prentice-Hall signal processing series (Prentice Hall, 1995).

[70] E. Bar-Ziv, Effect of diffraction on the moiré image. i. theory, *J. Opt. Soc. Am. A* **2**, 371 (1985).

[71] A. A. Ushkov, I. Verrier, T. Kampfe, and Y. Jourlin, Sub-wavelength diffraction gratings with macroscopic moiré patterns generated via laser interference lithography, *Opt. Express* **28**, 16453 (2020).

[72] R. Bistritzer and A. H. MacDonald, Moiré bands in twisted double-layer graphene, *Proc. Natl. Acad. Sci. USA* **108**, 12233 (2011).

[73] K. Kim, A. DaSilva, S. Huang, B. Fallahazad, S. Larentis, T. Taniguchi, K. Watanabe, B. J. LeRoy, A. H. MacDonald, and E. Tutuc, Tunable moiré bands and strong correlations in small-twist-angle bilayer graphene, *Proc. Natl. Acad. Sci. USA* **114**, 3364 (2017).

[74] H. Yoo, R. Engelke, S. Carr, S. Fang, K. Zhang, P. Cazeaux, S. H. Sung, R. Hovden, A. W. Tsien, T. Taniguchi, K. Watanabe, G.-C. Yi, M. Kim, M. Luskin, E. B. Tadmor, E. Kaxiras, and P. Kim, Atomic and electronic reconstruction at the van der waals interface in twisted bilayer graphene, *Nat. Mater.* **18**, 448 (2019).

[75] G. Tarnopolsky, A. J. Kruchkov, and A. Vishwanath, Origin of magic angles in twisted bilayer graphene, *Phys.*

Rev. Lett. **122**, 106405 (2019).

[76] D. Aggarwal, R. Narula, and S. Ghosh, A primer on twistronics: a massless dirac fermion's journey to moiré patterns and flat bands in twisted bilayer graphene, *J. Phys.: Condens. Matter* **35**, 143001 (2023).

[77] M. Saxena, G. Eluru, and S. S. Gorthi, Structured illumination microscopy, *Adv. Opt. Photon.* **7**, 241 (2015).

[78] F. Ströhl and C. F. Kaminski, Frontiers in structured illumination microscopy, *Optica* **3**, 667 (2016).

[79] A. Classen, J. von Zanthier, M. O. Scully, and G. S. Agarwal, Superresolution via structured illumination quantum correlation microscopy, *Optica* **4**, 580 (2017).

[80] S. Zhou, Y. Fu, X. Tang, S. Hu, W. Chen, and Y. Yang, Fourier-based analysis of moiré fringe patterns of superposed gratings in alignment of nanolithography, *Opt. Express* **16**, 7869 (2008).

[81] L. Kong, S. Cai, Z. Li, G. Jin, S. Huang, K. Xu, and T. Wang, Interpretation of moiré phenomenon in the image domain, *Opt. Express* **19**, 18399 (2011).

[82] O. Bryngdahl, Moiré: Formation and interpretation, *J. Opt. Soc. Am.* **64**, 1287 (1974).

[83] T. M. Radchenko, A. A. Shylau, I. V. Zozoulenko, and A. Ferreira, Effect of charged line defects on conductivity in graphene: Numerical kubo and analytical boltzmann approaches, *Phys. Rev. B* **87**, 195448 (2013).

[84] A. Ferreira, J. Viana-Gomes, J. Nilsson, E. R. Mucciolo, N. M. R. Peres, and A. H. Castro Neto, Unified description of the dc conductivity of monolayer and bilayer graphene at finite densities based on resonant scatterers, *Phys. Rev. B* **83**, 165402 (2011).

[92] J.-H. Chen, C. Jang, S. Xiao, M. Ishigami, and M. S. Fuhrer, Intrinsic and extrinsic performance limits of graphene devices on SiO₂, *Nature Nanotech* **3**, 206 (2008).

[86] O. Balci and C. Kocabas, Rapid thermal annealing of graphene-metal contact, *Appl. Phys. Lett.* **101**, 243105 (2012).

[87] F. Giubileo and A. Di Bartolomeo, The role of contact resistance in graphene field-effect devices, *Prog. Surf. Science* **92**, 143 (2017).

[88] P. G. Averbuch, Zero energy divergence of scattering cross sections in two dimensions, *J. Phys. A* **19**, 2325 (1986).

[89] H. Zoubi and G. C. La Rocca, Exciton-polariton kinematic interactions in organic microcavities, *Phys. Rev. B* **72**, 125306 (2005).

[90] V. Ngampruetikorn and J. A. Sauls, Impurity-induced anomalous thermal hall effect in chiral superconductors, *Phys. Rev. Lett.* **124**, 157002 (2020).

[91] D. K. Efetov and P. Kim, Controlling electron-phonon interactions in graphene at ultrahigh carrier densities, *Phys. Rev. Lett.* **105**, 256805 (2010).

[92] J.-H. Chen, C. Jang, S. Xiao, M. Ishigami, and M. S. Fuhrer, Intrinsic and extrinsic performance limits of graphene devices on SiO₂, *Nature Nanotech* **3**, 206 (2008).

[93] T. Sohier, M. Calandra, C.-H. Park, N. Bonini, N. Marzari, and F. Mauri, Phonon-limited resistivity of graphene by first-principles calculations: Electron-phonon interactions, strain-induced gauge field, and boltzmann equation, *Phys. Rev. B* **90**, 125414 (2014).